Effects of vermiculite on *in-situ* thermal behaviour, microstructure, physical and mechanical properties of fired clay bricks

Sen Wang [a, b, e], Lloyd Gainey [c], Julius Marinelli [c], Brianna Deer [c], Xiaodong Wang [a, b], Ian D. R. Mackinnon [b, d] and Yunfei Xi [a, b, e*]

[a] Central Analytical Research Facility (CARF), Queensland University of Technology (QUT), Brisbane, Queensland 4001, Australia

[b] Centre for Clean Energy Technologies and Practices & Centre for Materials Science, Queensland University of Technology (QUT), Brisbane, Queensland 4001, Australia

[c] Austral Bricks, Rochedale, Queensland 4123, Australia

[d] School of Earth and Atmospheric Sciences, Faculty of Science, Queensland University of Technology (QUT), Brisbane, Queensland 4001, Australia

[e] School of Chemistry and Physics, Faculty of Science, Queensland University of Technology (QUT), Brisbane, Queensland 4001, Australia

*Corresponding author

E-mail address: y.xi@qut.edu.au (Y. Xi)

Post address: Room 605C, Level 6, P block, Gardens Point Campus, Queensland University of Technology, Brisbane, QLD 4001, Australia

Abstract

Vermiculite is a hydrous clay mineral that occasionally occurs in raw materials for brickmaking. The presence of vermiculite affects the drying and firing processes of brick production; thus, the functions of this clay mineral should be clarified. In this study, vermiculite from 0 wt.% to 30 wt.% have been added to clay mixtures for brick button firing. Through effective integration of *in-situ* XRD, thermogravimetric and dilatometric analyses, the real-time thermal behaviours have been interpreted, and the microstructure, physical and compressive characteristics of brick buttons have been investigated. The incorporation of vermiculite has changed the temperatures of kaolinite dehydroxylation and rutile formation. Enstatite, cordierite and amorphous contents increased in fired brick buttons, while mullite, quartz and cristobalite decreased. Vermiculite retained a partial sheet-like morphology at 1150 °C firing. From 25-1150 °C, five weight loss steps have been defined with six shrinkage/expansion processes observed. Cracks appeared on brick button surfaces when 30 wt.% of vermiculite was added. The colour of fired brick buttons changed from “light camel” to “black olive”. Drying shrinkage, firing shrinkage and bulk density increased with an increased proportion of vermiculite. The maximum compressive strength reached 150.94 MPa (a rise of 21.6% towards the control sample) when 5 wt.% of vermiculite was added.

Keywords

Vermiculite; Fired clay brick; Compressive strength; Crack; Thermal behaviour; Thermal diffusivity

1. Introduction

Clays are the most widely distributed natural resources in the world and among the oldest building material ingredients throughout human history [1]. Bricks made of air-dried clays are reported to be used as early as the Neolithic period and fired clay bricks were made around 4500 BC [2]. Firing is crucial for brickmaking because it can vitrify clays and densify brick bodies. Brick porosity is significantly reduced during firing with an increase of mechanical strength. The produced vitreous phases are filled by mineral particles that results in a hard and insoluble ceramic product.

Since clays are natural materials with different origins, the clay minerals included in brickmaking vary in type and content. Importantly, although often used interchangeably by non-specialists, “clay” and “clay mineral” are two different concepts. Sedimentologists use “clays” to define particles smaller 4 μm, while mineralogists reserve the name clay minerals for specific classes of phyllosilicates informed by structure [1]. Traditionally, brick manufacturers only define clays based on their particle sizes ($\leq$ 2 μm) [3].

However, different clay minerals affect brick properties depending on crystal structures, elemental compositions, plasticity and shrinkage behaviours [4-7]. Defects may also occur in bricks (*e.g.*, cracking, bloating, and deformation) if inappropriate clay minerals or dosages are present in the starting materials. Thus, a comprehensive investigation of the relationship between clay minerals and the obtained brick characteristics is critical.

Vermiculite is a swelling hydrous phyllosilicate clay mineral with an ideal chemical formula of $(Mg^{2+}, Fe^{2+}, Fe^{3+})_3[(SiAl)_4O_{10}]OH_2 \cdot 4H_2O$ [8]. In nature, vermiculite usually coexists with interstratified vermiculite-biotite and/or biotite as a weathering or hydrothermal alteration product of biotite/phlogopite [9]. Since vermiculite can be expanded up to 30 times its original volume when heated at 650-950 °C, expanded vermiculite (EV) is often used as an additive in

cementitious materials and geopolymers to obtain higher porosity and fire resistance. However, compared with EV, natural vermiculite has rarely been studied for building material purposes, although in some cases, it appears in clays/shales used for brick manufacturing and is inferred to cause strength reduction due to intense expansion at high temperatures [10, 11].

To date, knowledge gaps on the function of natural vermiculite during brickmaking exist in three aspects: 1) most of the research focuses on EV rather than natural vermiculite [12-14]; 2) lack of an effective combination of modern characterisation techniques to reveal effects of vermiculite on the whole brick production process and brick properties [11]; 3) lack of research on the positive impact of high-temperature expansion from vermiculite during brickmaking; for example, whether this expansion can offset the shrinkage of other phases to promote improved brick performance. A lack of this knowledge makes it challenging to obtain a practical reference point for industrial brick production, which can cause economic loss due to vermiculite-related defective products.

In this study, natural vermiculite was used as an additive to make clay brick specimens. The influence of vermiculite on *in-situ* thermal behaviour, microstructure, physical and mechanical properties of fired brick buttons has been investigated. The main objective is to reveal the changes and corresponding mechanisms when vermiculite is present in brickmaking and provide suggestions for enhanced industrial production of higher-performing building materials.

2. Materials and methods

2.1. Raw material and sample preparation

A clay mixture (CM) and vermiculite (V) were collected from a local brick manufacturer in Queensland, Australia. CM consists of five pit clays/shales extracted from the Late Permian and Triassic coal basins in Queensland. These clays/shales are abundant in clay minerals which

were altered from granite and tuff. Less than 5 wt.% of perlite and brick grogs are also incorporated in CM as a routine practice by the local industry. Vermiculite was obtained from a commercial supplier without heating and exfoliation treatment.

Before use, both CM and V were dried at 40 °C for 24 h, then crushed in a laboratory ring mill until they could pass a 160 µm sieve. The initial moisture contents of CM and V were 1.32 wt.% and 3.93 wt.%, respectively, and these values were reduced to 0.58 wt.% and 3.32 wt.% after drying, respectively (via measuring the mass loss after heating at 105 °C for 12 h). The mixing design of CM, V and water is shown in **Table 1**. Firstly, the required amounts of CM and V were mixed in a 100 ml glass beaker. After manually stirring for 10 mins (using a metal spatula to homogenise the sample), 4 ml of water was added utilising a pipettor (NEXTY 1000). The mix was set aside for ~10 mins to allow water to diffuse. Then, another 5 mins of manual stirring was conducted, and the mix was pressed under 5 tons for 2 mins using a hydraulic press. Shaped and undried buttons were obtained, including CM, CMV5, CMV10, CMV20 and CMV30 (called green buttons). Each button has a diameter of 4 cm and a thickness of ~2 cm. Also, five samples per series were prepared to enable comparative and statistical results.

Sample ID	CM (g)	V (g)	Water (ml)
CM	40.0	0.0	4.0
CMV5	38.0	2.0	4.0
CMV10	36.0	4.0	4.0
CMV20	32.0	8.0	4.0
CMV30	28.0	12.0	4.0

Table 1. Recipes for sample mixing

The green buttons were dried at 110 °C for 24 h. Then, the dried buttons were fired in a Carbolite Gero AAF 11/3 furnace at 1150 °C, with the heating rate and soaking time of 5 °C/min and 2 h, respectively. A firing temperature of 1150 °C (rather than 950 °C) was chosen because it is designed for Queensland clays which are rich in well-crystallised clay

minerals but have fewer fluxes. This higher temperature is routinely used by brick manufacturers in Queensland, Australia.

2.2. Characterisation methods

X-ray diffraction (XRD) patterns were acquired using a Bruker D8 Advance diffractometer (Co Kα, 35 kV, 40 mA) from 2° to 90° 2θ at a step size of 0.02° and a scan speed of 1.5° 2θ/min. A 10 wt.% internal standard (corundum) was used for quantitative phase analysis. To determine swelling clay minerals in CM, gravity sedimentation experiments were applied to prepare clay slides for XRD measurement: A small portion of the crushed samples was dispersed in deionised water. A few drops of concentrated ammonia were added. After sonication for 5 min and settling for 20 min, the fine fraction (nominally < 5 μm in suspension) was transferred via pipette to a Si *511* low background plate. Oriented clay sample mounts were treated under three different conditions: (i) air drying, (ii) ethylene glycol treatment, and (iii) heating at 550 °C for 2 h.

For *in-situ* XRD measurements on CM and CMV30 samples, a Rigaku Smartlab X-ray diffractometer (Cu Kα, 40 kV, 40 mA) equipped with an Anton Paar HTK-1200N chamber and a Rigaku Reactor-X chamber were used. XRD patterns were collected from 3° to 45° 2θ at a step size of 0.02°. The temperature was increased from 30 °C to 1150 °C with a ramp rate of 5 °C/min under 100 mL/min dry airflow. The sample height was aligned at each temperature to prevent expanded sample holder height compromising XRD reflections. Phase identification of the XRD pattern was conducted in DIFFRAC.EVA v5 in ICDD PDF-4+ 2021 database. Quantitative Phase Analysis was conducted in DIFFRAC.TOPAS v6, using an internal standard method. The bulk chemical compositions of clay samples were measured using a PANalytical AXIOS 1kW wavelength dispersive X-ray fluorescence (XRF) spectrometer.

Losses on ignition (LOI) were calculated before and after calcination at 1050 ℃ for 2 h in a Carbolite Gero AAF 11/3 furnace.

Thermogravimetric analysis (TGA) was undertaken on dried brick buttons (dried CM, CMV5, CMV10, CMV20, CMV30, fine powders) using a Netzsch STA 4493F from 25 ℃ to 1150 ℃ at 5℃/min in 100 mL/min airflow, then an isothermal condition was kept at 1150 ℃ for 2 h. The N_2 isothermal absorption and desorption measurement was run using a Tristar II 3020 with a 99-point Brunauer-Emmett-Teller (BET) method. Approximately 1.0 g of fired samples (fired CM, CMV5, CMV10, CMV20 and CMV30, fine powders) were degassed at 150 ℃ for 24 h before the test. The average pore size was estimated by the Barrett-Joyner-Halenda (BJH) method on the desorption branch.

The surface morphologies of fired brick buttons (fired CM and CMV30) were imaged using a field emission scanning electron microscope (FESEM, JEOL 7001F) using backscattered electron (BSE) imaging. An X-Max 80 (Oxford, UK) energy-dispersive X-ray spectroscopy (EDS) system was applied to determine elemental compositions. Sample preparation procedures are shown in the Supplementary document.

For thermal dilatometric tests, small rectangular bars (2 x 0.5 x 0.5 cm) were cut from brick buttons (dried CM, CMV5, CMV10, CMV20 and CMV30) and measured in a Netzsch 402C dilatometer. The same heating program and atmosphere were used as those in the *in-situ* XRD and TGA measurements. Thermal diffusivity was measured on brick disks (Φ1 x 0.5 cm) using a Netzsch LFA 467 light flash apparatus. Drying and firing shrinkages were determined on the diameter changes of brick buttons. Ten positions were selected and the average value was calculated. The 24-h cold water absorption, 5-h boiled water absorption and compressive strength were conducted according to ASTMC67/C67M [15].

3. Results and discussion

3.1. Characterisation of raw materials

Elemental compositions of CM and V were measured by XRF, and the results are shown as oxides in **Table 2**. CM contains a significant amount of SiO_2 (60.09%), mainly originating from quartz and clay minerals, as confirmed by the XRD pattern in **Fig. 1a**. Al_2O_3 accounts for 22.12% in CM, followed by reduced concentration of fluxes - Fe_2O_3 (2.93%), K_2O (1.30%), TiO_2 (0.86%), MgO (0.52%) and MnO (0.02%). A small amount of CaO (0.76%) has also been detected, attributed to calcite microfacies identified by XRD (**Fig. 1a**). CM can be classified as a non-calcareous and low refractory clayey material with CaO and flux no more than 6.00% and 9.00%, respectively [16].

	SiO_2	Al_2O_3	Fe_2O_3	TiO_2	CaO	MnO	K_2O	MgO	Na_2O	BaO	P_2O_5	SO_3	LOI.
CM	60.09	22.12	2.93	0.86	0.76	0.02	1.30	0.52	0.18	0.04	0.04	0.06	10.76
V	37.71	8.39	8.37	0.99	4.97	0.07	5.04	21.71	0.06	0.07	2.00	0.02	10.60

Table 2. Elemental analysis of principal oxides (in wt.%) in raw materials

According to the XRD patterns (**Fig. 1a** and **Fig. S1a** in the supplementary material), kaolinite [PDF 00-058-2004, index (001) at 7.14 Å 2θ], quartz [PDF 04-012-0490, index (101) at 3.34 Å], illite/mica [PDF 04-014-1813, index (002) at 9.90 Å] and mixed-layer illite-smectite are four major minerals in CM. 9.90% of amorphous phase also exists, followed by trace amounts of microcline [PDF 01-071-0955, index (040) at 3.24 Å], mullite [PDF 04-016-1588, index (110) at 5.37 Å], anatase [PDF 04-001-7641, index (101) at 3.52 Å], cristobalite [PDF 04-008-7742, index (101) at 4.04 Å], calcite [PDF 01-083-4601, index (104) at 3.03 Å] and albite [PDF 00-009-0466, index (002) at 3.19 Å] (**Fig. 1b**). Generally, mullite is a high-temperature phase uncommon in natural clay. Mullite in CM is mainly derived from the added 2.5% of brick grogs.

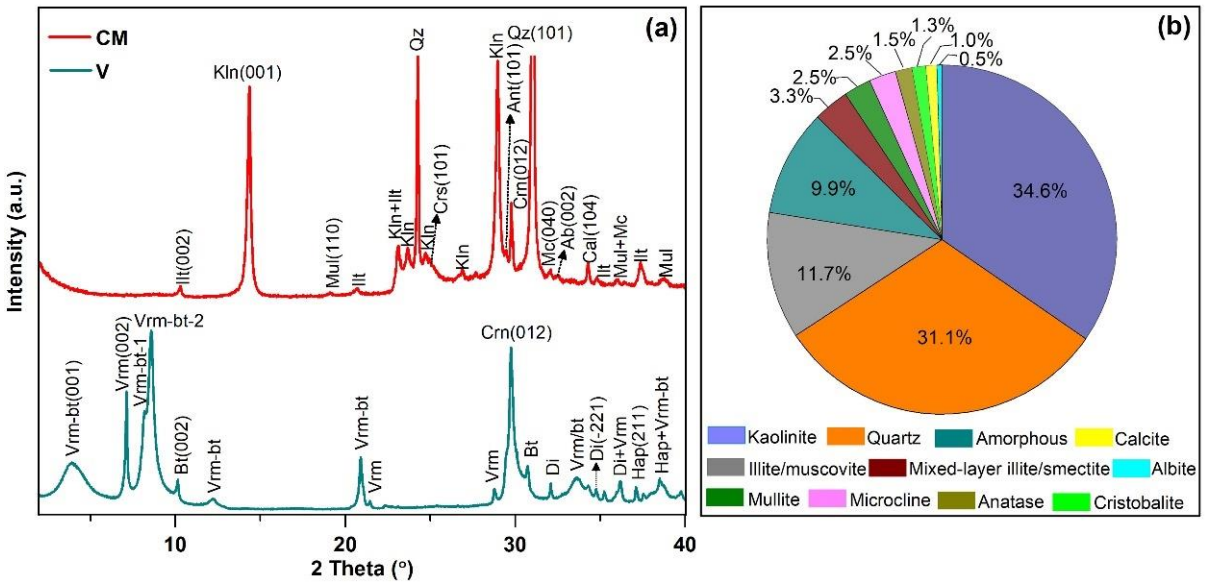

Fig. 1. XRD patterns of CM and V (**a**) and quantitative XRD result of CM (**b**). Legend: Vrm-bt-vermiculite-biotite, Vrm-vermiculite, Bt- biotite, Ilt-illite/mica, Kln-kaolinite, Mul-Mullite, Qz-quartz, Crs-cristobalite, Crn-corundum, Ant-anatase, Mc-microcline, Ab-albite, Cal-calcite, Di-diopside, Hap-hydroxyapatite. Mineral abbreviations after [17]

Compared to CM, V exhibits distinct chemistry with SiO_2 making up only 37.71%. A lower SiO_2 content in V is due to the absence of quartz (**Fig. 1a**). Also, MgO occupies 21.71% with minor proportions of Al_2O_3 (8.39%), Fe_2O_3 (8.37%) and K_2O (5.04%). These elements are consistent with predominant vermiculite [PDF 01-077-0022, index (002) at 14.47 Å], interstratified vermiculite-biotite (vrm-bt) [PDF 00-049-1057, index (001) at 26.66 Å] and biotite [PDF 04-013-2135, index (002) at 10.16Å] in V. CaO (4.97%) and P_2O_5 (2.00%) are consistent with a hydroxyapatite phase [PDF 01-073-7582, index (211) at 2.82 Å]. According to **Fig. 1(a)** and **Fig. S1b**, V contains two different vrm-bt (marked as vrm-bt-1 and vrm-bt-2) linked to (002) reflections at 12.5 Å and 11.9 Å, respectively. These two vrm-bt may consist of different orders between vermiculite and biotite; thus, slightly different reflection positions are observed in the XRD patterns. However, the quantitative phase analysis of V has not been conducted due to the lack of crystal structure models for these two interstratified vrm-bt.

3.2. Real-time phase transformation

For *in-situ* XRD patterns (**Fig. 2a** and **2b**), three humps centred at 4.4°, 6.7° and 13.5° 2θ are from the Kapton and graphite window material of the HTK-1200N chamber, not associated with our samples. Conventional waterfall images of *in-situ* XRD patterns of CM and CMV30 are also shown in **Fig. S2**. Since the 6.7° 2θ hump overlaps with vermiculite and vrm-bt reflections in the low-temperature region (**Fig. 2b**), another batch of *in-situ* XRD patterns was collected using a Rigaku Reactor-X chamber equipped with a beryllium window up to 700 °C to eliminate this interference (**Fig. 2c**).

In sample CM, kaolinite and illite/mica dehydroxylate at 430-625 °C and 625-820 °C, respectively (**Fig. 2a**). The (001) reflection of kaolinite disappears after dehydroxylation, while illite/mica retains the (002) reflection until 980 °C. This difference is caused by distinct changes of Al coordination during dehydroxylation [18, 19]. Since kaolinite shows a 1:1 type layer structure consisting of one Si-tetrahedral layer and one Al-octahedral layer, the Al-octahedron in kaolinite migrates into the inter-layer spacing during dehydroxylation, resulting in a distortion of the 1:1 Al-Si layers; thus, a loss of crystallographic order [6]. As for illite/mica, two Si-tetrahedra in the 2:1 layer structure may well stabilise the middle Al-octahedron during dehydroxylation. Thus, Al atoms in octahedral sheets may combine with remaining oxygen atoms to achieve fivefold coordination. The newly formed illite/mica-anhydride presents long-range order, so the XRD reflection of the (002) plane remains.

At 460-660 °C, quartz shifts its reflections to lower angles due to a transition from α- to β-phase (**Fig. 2a**). This process is reversible, and microcracks may develop at this time both in the heating up and cooling down processes due to a larger expansion/shrinkage coefficient of quartz compared to its neighbouring phases. In industrial brick production, a slower ramping rate is necessary to avoid a “dunting” problem. After 660 °C, the $d_{(101)}$ value of β-quartz drops

slightly because of crystal contraction along the *c*-axis [6, 20]. This value increases again when the temperature reaches 1150 °C and remains stable until the end of the heating protocol.

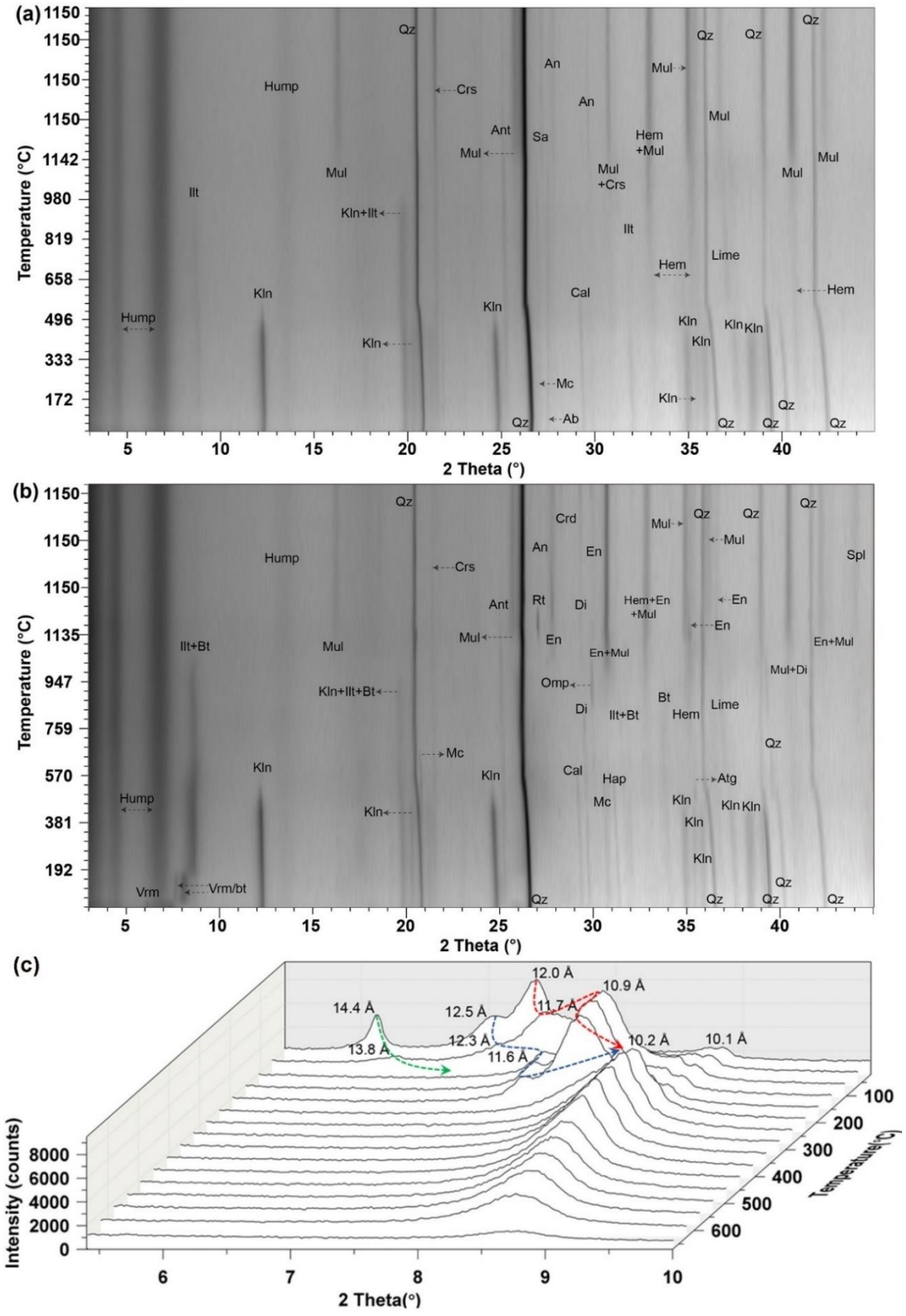

Fig. 2. 2D *in-situ* XRD patterns of CM (**a**), CMV30 (**b**), and supplementary *in-situ* XRD patterns of CMV30 using the Reactor-X chamber (**c**). Green, blue and red arrows represent evolution of reflections for vrm, vrm-bt-1 and vrm-bt-2 with temperature, respectively. Legend: Vrm-bt-vermiculite-biotite, Vrm-vermiculite, Ilt-illite/mica, Kln-kaolinite, Mul-Mullite, Qz-quartz, Crs-cristobalite, Crn-corundum, An-anorthite, Ant-anatase, Mc-microcline, Hem-hematite, Omp-omphacite, Sa-sanidine, Ab-albite, Cal-calcite, Di-diopside, Hap-hydroxyapatite, Rt-rutile, En-enstatite, Crd-cordierite, Spl-spinel, Atg-antigorite. Mineral abbreviations after [17]

At ~590 °C, calcite decomposes into lime (PDF 01-077-9574, CaO) in CM as a result of the following reaction:

$$CaCO_3(\text{calcite}) \rightarrow CaO(\text{lime}) + CO_2 \quad (1)$$

The (200) reflection of lime can be seen at around 37.3° 2θ (2.40 Å) in **Fig. 2a**. However, the onset temperature of this reaction is lower than previous research [21], which demonstrates that calcite decomposed between 700 and 800 °C. It is worth clarifying that a few factors may influence the decomposition of calcite, such as sample quantity, particle size, foreign materials, heating rate, CO_2 partial pressure, gaseous environment and purge gas velocity [22, 23]. Spinolo and Anselmi-tambuini [24] also reported the low-temperature decomposition of calcite at 546-596 °C, which is consistent with this study.

Although a few literature studies have demonstrated the presence of Ca-related silicate/aluminosilicate in fired bricks, *e.g.*, gehlenite [$Ca_2Al(AlSiO_7)$], diopside ($CaMgSi_2O_6$) and wollastonite ($CaSiO_3$) [25, 26], these minerals are not observed in this study except for a small amount of anorthite (PDF 01-076-0832, $Ca_{0.86}Na_{0.14}Al_{1.84}Si_{2.16}O_8$). The possible reason is well explained by the XRF data in **Table 2**, where only 0.76% of CaO is present in CM. In addition, with an increase of temperature, hematite (PDF 01-089-8103, Fe_2O_3) forms at 690 °C

with an enhanced reflection identified at 2.42 Å (~37.1° 2θ, indicated by darker colour in **Fig. 2a**). Fe in hematite is inferred from illite/mica during its dehydroxylation process when Fe site distortion increases and Fe ions are released.

Regarding the feldspar family, microcline diminishes in concentration after 980 °C and does not present when T > 1140 °C (**Fig. 2a**). A possible explanation is a transformation from microcline to sanidine (PDF 01-087-0680, $K_{0.86}Na_{0.14}AlSi_3O_8$) at high temperatures [21]. The (-202) reflection of sanidine appears only after 1045 °C (**Fig. 2a**), indicating a slow crystallisation process. In addition, the microcline likely alters to anorthite with the participation of lime, given the development of the anorthite (0-22) reflection from 980 °C (**Fig. 2a**). The Na-rich plagioclase feldspar - albite remains in CM until melting at 1150 °C.

For high-temperature related phases, trace amounts of mullite and cristobalite are present even from room temperature in **Fig. 2a**. After 980 °C, mullite becomes noticeable through crystallisation of clay minerals as a result of the following reactions [21, 27-29]:

$$Al_2Si_2O_7(\text{metakaolin}) \rightarrow 0.67Al_6Si_2O_{13}(\text{mullite}) + 2.67SiO_2(\text{amorphous}) \quad (2)$$

$$3KAl_2Si_3AlO_{11}(\text{illite/mica-anhydride, theoretical formula}) + 2SiO_2 \rightarrow 3KAlSi_3O_8(\text{sanidine}) + Al_6Si_2O_{13}(\text{mullite}) \quad (3)$$

$$\text{Illite/mica} \rightarrow 0.275\text{mullite} + 0.667\text{melt} + 0.244K_2O + 0.01Na_2O + 0.125H_2O \quad (4)$$

An increase of cristobalite occurs at 1150 °C, which is produced by modification of β-quartz. Parts of cristobalite may also come from amorphous SiO_2 generated in Equation 2. Furthermore, the presence of anatase is evident throughout the entire temperature range.

After the addition of V by 30 wt.%, the mineralogical transformation in the clay mixture significantly changes with the formation of new phases.

Clay minerals: The $d_{(002)}$ of vermiculite changes from 14.4 Å (45 °C) to 13.8 Å (85 °C) with firing proceeding (**Fig. 2c,** green arrow), then it overlaps with the reflection of vrm-bt-1 at T > 130 °C. The $d_{(002)}$ values of vrm-bt-1 and vrm-vt-2 decrease first, then stabilise at ~10.2 Å at 250 °C (**Fig. 2c**), when the dehydrated state in the interlayer space of vermiculite forms. The removal of two-layered bound water molecules in vrm-bt-1 are recorded by sudden drops of $d_{(002)}$ from 12.3 to 11.6 Å (85-125 °C) and 11.6 to 10.2 Å (210-250 °C) (**Fig. 2c**, blue arrow). A similar evolution can also be seen in vrm-bt-2 (**Fig. 2c**, red arrow**)**. With an increase in temperature, the reflections of both vermiculite and vrm-bt become broader, indicating a lower degree of crystallinity. This result is consistent with vermiculite data in [30]. The minor reflection contributed by biotite at about 10.1 Å (**Fig. 2c**) is almost unchanged during the vermiculite dehydration process.

In terms of other clay minerals, the onset temperature for kaolinite dehydroxylation drops from 430 to 415 °C in CMV30 (**Fig. 2b**). This is attributed to increased K^+ and Ca^{2+} in the clay mixture after V addition [31]. In addition, the reflection at 10.2 Å vanishes at 80 °C higher in CMV30 than that in CM due to the contribution of dehydroxylated vermiculite, biotite and vrm-bt (**Fig. S2a** and **S2b**).

Mg-related silicates/aluminosilicates: The newly formed Mg-related silicates/aluminosilicates in CMV30 include antigorite [PDF 04-017-4304, $Mg_{39}Si_{28}O_{70}(OH)_{50}$], enstatite (PDF 04-014-8123, $Mg_{0.69}Fe_{0.2}Al_{0.22}Si_{0.88}O_3$), cordierite (PDF 04-013-9145, $Na_{0.09}Mg_{1.82}Fe_{0.21}Al_4Si_5O_{18}$) and spinel (PDF 04-006-2474, $MgFe_{0.6}Al_{1.4}O_4$). The last three phases were also reported by Valášková et al. [32] after firing a mixture of kaolinite and vermiculite. However, Sutcu [13] identified none of these phases when expanded vermiculite was added into clay mixtures and fired at 900 °C and 1000 °C. It is speculated that vermiculite and expanded vermiculite may result in different phases when heated, or the neighbouring minerals can affect phase evolutions at high temperatures.

Minor Fe exists in these Mg-containing minerals due to the common substitution of Mg to form solid solutions. This is consistent with the XRF result (**Table 2**), showing high Mg and Fe contents in V. The EDS data below also provides evidence of Mg and Fe in cordierite and enstatite.

In **Fig. 2b**, antigorite occurs at ~460 °C at ~35.4° 2θ, after kaolinite dehydroxylation begins. The dehydroxylation releases H_2O molecules, which dissolve Mg and Si to form antigorite and result in 13 wt.% -OH groups in this mineral. At 870 °C, enstatite is crystallised from vermiculite [32]:

$$2Mg_3(Si_3Al)O_{10}(OH)_2(\text{vermiculite}) \rightarrow 6MgSiO_3(\text{enstatite}) + Al_2O_3 + H_2O \quad (5)$$

Then, cordierite and spinel form at 1150 °C [33]:

$$3MgSiO_3(\text{enstatite}) + Al_6Si_2O_{13}(\text{mullite}) \rightarrow Mg_2Al_4Si_5O_{18}(\text{cordierite}) + MgAl_2O_4(\text{spinel}) \quad (6)$$

Equations (5) and (6) are ideal reactions in the absence of Fe.

Other phases: Diopside transforms to omphacite (PDF 04-024-2679, $Na_{0.48}Ca_{0.49}Mg_{0.45}Fe_{0.07}Al_{0.54}Si_{1.97}O_6$) at 800 °C due to partial substitution of Ca and Mg by Na and Al. Anatase changes to rutile (PDF 04-006-1890, TiO_2) at 1100 °C. The evolution of anatase in CMV30 is different to that in CM. The appearance of rutile is attributed to a larger amount of K^+ and Fe^{3+} in CMV30, which can enter into the anatase lattice and increase the level of oxygen vacancy, thus, promoting the transformation from anatase to rutile [34]. Quantitative mineralogical analyses by Rietveld refinement are shown in **Fig. S3b** based on the XRD patterns of fired clay brick buttons (**Fig. S3a**),

3.3. Thermogravimetric study

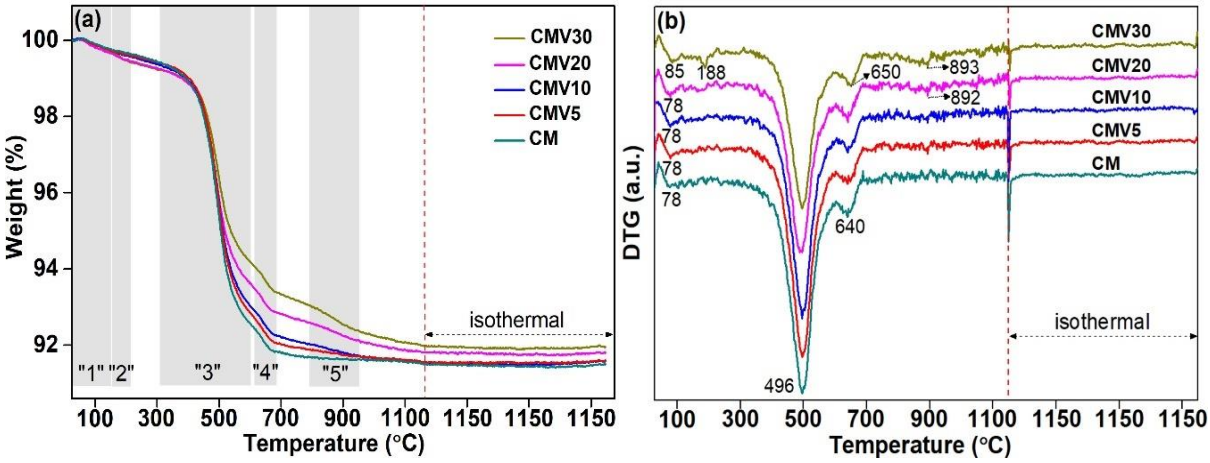

Fig. 3. Thermograms of clay mixtures: TGA (**a**) and DTG (**b**)

Five shaded areas have been highlighted in **Fig. 3a**, which represent different stages of weight loss. The corresponding DTG peaks have also been identified in **Fig. 3b**.

At around 80 °C, the first DTG peak for all samples is caused by removing hygroscopic water, especially from clay minerals with a relatively large specific surface area considering the starting mineral assemblage. The corresponding weight loss (area "1") slightly increases from 0.29 wt.% (CM) to 0.31 wt.% (CMV5), 0.32 wt.% (CMV10), 0.36 wt.% (CMV20) and 0.40 wt.% (CMV30). This can be explained by increasing vermiculite, vrm-bt and biotite in starting materials. In addition, vermiculite and vrm-bt are expected to have lost the first hydration spheres associated with interlayer cations during this period. At 188 °C (area "2"), only CMV30 exhibits a DTG peak in **Fig. 3b**, caused by removing the remaining hydration spheres from vermiculite and vrm-bt interlayer. Ma et al. [30] also observed a similar weight loss but at a higher temperature of 210 °C. The two weight losses of vermiculite and vrm-bt before 200 °C correspond well to the evolution of XRD basal reflections (**Fig. 2c)**.

As sample temperature is increased, the largest weight loss appears between 310-610 °C (area "3", **Fig. 3a**), attributed to a combined effect of kaolinite dehydroxylation and calcite decomposition. This weight loss is also confirmed by the *in-situ* XRD patterns (**Fig. 2a** and **2b**) and literature [35, 36]. The total weight losses in this temperature range are reduced from CM

(6.89 wt.%) to CMV5 (6.64 wt.%), CMV10 (6.40 wt.%), CMV20 (5.54 wt.%) and CMV30 (4.97 wt.%), attributed to diluted concentrations of kaolinite and calcite after V addition. In CM, 34.6 wt.% of kaolinite and 1.0 wt.% of calcite (**Fig. 1b**) should cause 4.84 wt.% and 0.44 wt.% of weight losses, respectively, as calculated by the theoretical formula of these two minerals. A total value of 5.28 wt.% loss is estimated, which is lower than the observed value (6.89 wt.%) by TGA data. Therefore, other clay minerals, *e.g.*, illite-smectite, are likely to dehydroxylate in this temperature range. Furthermore, organic impurities in clay burn out between 300-500 °C [37].

The area "4" in **Fig. 3a** is related to the dehydroxylation of both illite/mica and vermiculite in relative proportions. The dehydroxylation of illite/mica is observed on the *in-situ* XRD pattern in **Fig. 2a**. The DTG peak moves from 640 °C to 650 °C from CM to CMV30 (**Fig. 3b**) as vermiculite dehydroxylates at higher temperature (at 663 °C, **Fig. S4a**) than illite/mica. The wide DTG peaks at ~890 °C in CMV20 and CMV30, corresponding to the area "5" in **Fig. 3a**, are caused by the formation of enstatite from vermiculite with severe structural degradation and loss of -OH groups. This reaction is also confirmed by the *in-situ* XRD data (**Fig. 2b**) and the TGA result by [30]. When the temperature climbs to 1150 °C, isotherm begins and lasts for 2 h. Weights of all clay mixtures become nearly stable during this period since all moisture and gases (e.g. CO_2 and SO_2) have almost been released before 1150 °C. In general, ~8.00 wt.% has been lost by all samples during firing. The addition of V slightly reduces the total weight loss from 8.51 wt.% (CM) to 8.47 wt.% (CMV5), 8.42 wt.% (CMV10), 8.19 wt.% (CMV20) and 8.04 wt.% (CMV30).

3.4. Thermal dilatometric analysis

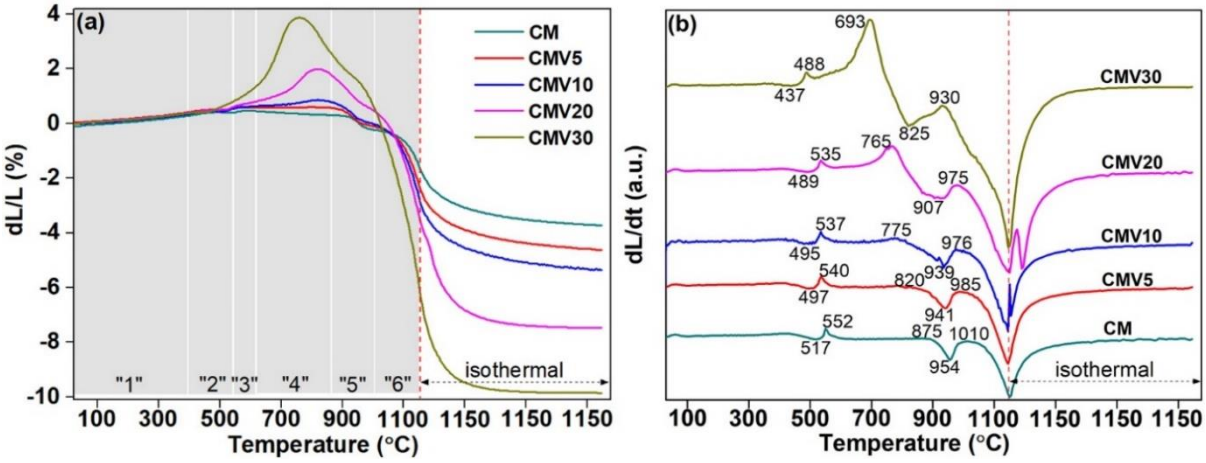

Fig. 4. Dilatometric curves (**a**) and the first derivative (dL/dt) curves (**b**) of clay mixtures

The addition of V has significantly changed the mineralogy and chemistry of the starting materials and resulted in different dimensional changes with increase of temperature. Six areas have been defined on the thermal dilatometric curve of CM (**Fig. 4a**). These areas slightly shift with V addition which can be explained by a few phase transition processes below:

Area "1" (25-375°C): The linear expansion during this period represents a steady enlargement of the unit cell with increased temperature. The length change for all clay bars is ~0.45%.

Area "2" (375-540 °C): The slight shrinkage is attributed to the dehydroxylation of kaolinite. *In-situ* XRD pattern in **Fig. 2b** also shows that kaolinite dehydroxylates at 430-625 °C. This shrinkage shifts from 517 °C (CM) to a lower temperature of 437 °C (CMV30) with the increased proportion of V in the green body (**Fig. 4b**). Dehydroxylation results in buckling or distortion of the kaolinite lamella. The two adjacent Al-Si (octahedral-tetrahedral) layers gradually link together to make the obtained metakaolin layers approximatively a double-thickness of kaolinite layers [38]. The interlayer spaces have been notably compressed/reduced in this process and contraction occurs.

Area "3" (540-605 °C): For CM, area "3" is related to the expansion by α- to β-quartz inversion and shrinkage by continuing dehydroxylation of kaolinite (**Fig. 2a**). The peak value at 552 °C

is ~20 °C lower than the theoretical temperature of quartz inversion (573 °C), which is possibly caused by impurity atoms in natural quartz, *e.g.*, Al, Ti and Fe [39]. The dL/dt peaks appear at lower temperatures with increased V content (**Fig. 4b**). Noticeable length increases (particularly in CMV30) are also observed due to the expansion/exfoliation of vermiculite and vrm-bt at above 450 °C. The onset temperature corresponds well with the result by Muiambo et al. [40]. Detailed mechanisms are discussed in area "4" below.

Area "4" (605-875 °C): CM contracts by 0.14% while the other samples expand by 0.01% (CMV5), 0.16% (CMV10), 1.27% (CMV20) and 3.19% (CMV30) (**Fig. 4a**). The dimensional variations are due to the following reactions/changes:

1) Expansion and exfoliation of vermiculite and vrm-bt;
2) Vermiculite peels when the force generated by the internal steam pressure exceeds the interlayer ionic bonding force. The rapid expansion in area "4" is caused by severe exfoliation of interstratified vrm-bt combined with a slight volumetric increase of vermiculite. Interstratified vrm-bt displays a much higher expansion coefficient than neat vermiculite after "flash" heating. The mosaic-like arrangement in vrm-bt can act as a maze for escaping vapour and provide more dead-end sites [10]. A build-up of pressure at these sites results in higher forces to impact the lamellar structure, and consequently, more significant expansion. Condensation of residual hydroxyls and collapse of metakaolin occurs.

   The dehydroxylated kaolinite (metakaolin) still has a minor amount of -OH groups as a result of the following reaction:

   $$[(OH)_8](\text{kaolinite}) \rightarrow [OH+3.5O](\text{metakaolin}) + 3.5H_2O \quad (7)$$

   These residual -OH groups are gradually lost at ~605-860 °C, accompanied by a slight shrinkage of clay. In addition, after dehydroxylation, the coordination of Al in metakaolin is changed to 4- or 6-fold for the formation of a short-range order

material - the precursor of mullite [41]. The original crystal lattice of metakaolin collapses, then the clay shrinks;

3) Dehydroxylation of illite/mica and biotite

In-situ XRD and TGA depict that dehydroxylation of illite/mica and biotite occur at 625-820 °C with the crystal structures maintained. Slight structural expansions may happen in these phases as inferred by increased $d_{(002)}$ values at~10.2 Å (**Fig. 2**);

4) A gradual contraction of β-quartz with the rising temperature [20].

Area "5" (875-1010 °C): The linear shrinkage of ~0.56% (CM, **Fig. 4**) corresponds to mullite crystallisation from metakaolin due to Equation 2. Illite/mica and mixed layer illite-smectite also collapse and cause a small amount of contraction during this period [42]. The peak temperature decreases from 954 °C (CM) to 941°C (CMV5), 939 °C (CMV10), 907 °C (CMV20) and 825 °C (CMV30) with V addition. This change can be explained by the proportion of enstatite crystallisation that displays a low-temperature peak at 823°C as indicated by TGA data in **Fig. S4b**. Besides, the addition of V notably enhances the shrinkage during this period. A ~2.1% length reduction is observed in sample CMV30, approximatively three times larger than that in CM.

Area "6" (1010-1150 °C): The contraction in CM is caused by the crystallisation of mullite from illite/mica and mixed layer illite-smectite. A viscous glass-type liquid occurs at this temperature as it segregates from the decomposition products [43]. The corresponding dL/dt peak gradually widens and becomes asymmetric with an increase in V content. This change is due to an overlap of the 1016 °C and 1137 °C peaks related to the dehydroxylation of biotite and the subsequent melting of biotite, vrm-bt and vermiculite particles, respectively (**Fig. S4b)**. The clay minerals in V have considerably promoted the vitrification process during this process, so denser structures are finally obtained. The residual length of each clay bar after dilatometry

measurement is: 96.27% (CM), 95.38% (CMV5), 94.63% (CMV10), 92.52% (CMV20) and 90.15% (CMV30).

3.5. Morphology and microstructure

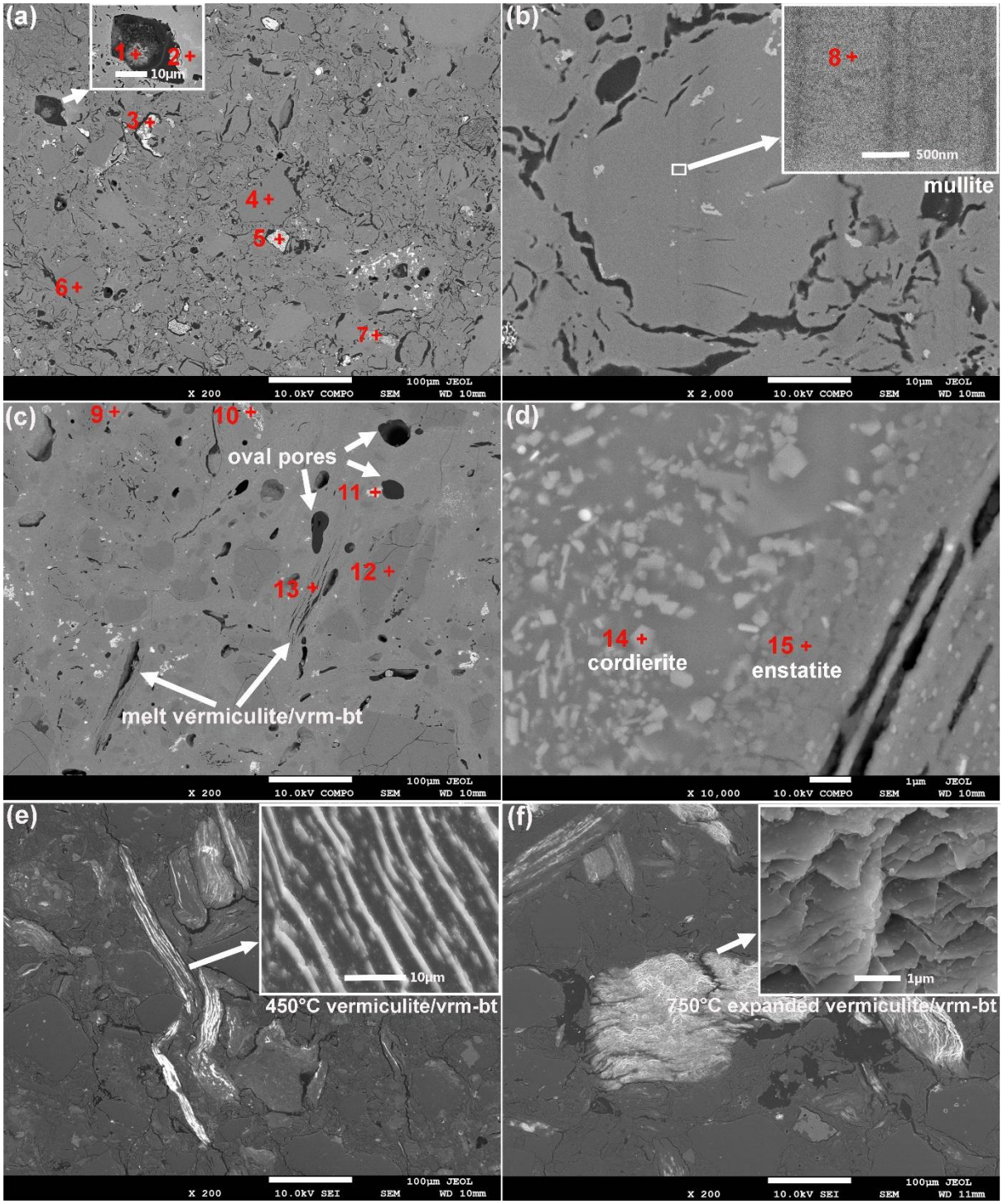

Fig. 5. BSE images of fired brick buttons: fired CM button at 1150 °C (**a**) and (**b**), fired CMV30 button at 1150°C (**c**) and (**d**), fired CMV30 button at 450 °C (**e**) and 750 °C (**f**); Insets: higher magnification images of decomposed calcite (**a**), mullite (**b**), un-expanded/un-exfoliated vermiculite/vrm-bt (**e**) and expanded/exfoliated vermiculite/vrm-bt (**f**)

For the fired CM brick button, micron-sized cracks/pores appear in the mineral/amorphous matrix. The large pore with irregular shape (white arrow, **Fig. 5a**) might be caused by the decomposition of calcite and release of CO_2, as confirmed by the *in-situ* XRD pattern in **Fig. 2a.** Ca is therefore enriched inside the pore (point 1, **Fig. 5a**), which gives rise to Ca-related silicate/aluminosilicate formation at the pore edge, *e.g.*, anorthite (point 2, **Fig. 5a**). According to the EDS results (**Table 3**), the identified minerals in the fired CM brick button are hematite (points 3 and 5), quartz/cristobalite (points 4 and 6) and anatase (point 7). Microcrystalline mullite is also observed at higher magnification (**Fig. 5b**) with a low K and Ca contents in composition (point 8, **Table 3**).

Element	Element concentration of points measured by EDS (atom%)														
	CM fired button								CMV30 fired button						
	1	2	3	4	5	6	7	8	9	10	11	12	13	14	15
O	58.6	61.6	50.3	66.7	50.3	66.7	66.1	58.3	60.0	66.5	51.1	66.6	59.8	59.6	60.6
Si	12.0	16.4	0.3	33.3	0.3	33.3	3.9	10.1	20.0	0.2	1.2	33.0	17.0	12.3	18.4
Al	9.0	13.7	0.5	n.d.	0.5	n.d.	1.6	30.8	24.3	0.5	2.1	0.4	4.5	14.8	6.1
Fe	4.0	0.9	48.8	n.d.	48.8	n.d.	n.d.	n.d.	1.0	n.d.	45.5	n.d.	2.1	4.1	1.6
Ca	12.3	7.1	n.d.	n.d.	n.d.	n.d.	0.3	0.1	9.7	n.d.	n.d.	n.d.	n.d.	0.3	0.3
Mg	1.0	0.2	n.d.	n.d.	n.d.	n.d.	0.2	n.d.	9.2	0.3	n.d.	n.d.	16.3	7.8	11.9
K	n.d.	n.d.	n.d.	n.d.	n.d.	n.d.	0.3	0.7	n.d.	n.d.	n.d.	n.d.	n.d.	1.1	0.8
Na	n.d.	n.d.	n.d.	n.d.	n.d.	n.d.	n.d.	n.d.	n.d.	n.d.	n.d.	n.d.	n.d.	n.d.	n.d.
Ni	2.1	n.d.	n.d.	n.d.	n.d.	n.d.	n.d.	n.d.	n.d.	n.d.	n.d.	n.d.	n.d.	n.d.	n.d.
Ti	0.4	n.d.	n.d.	n.d.	n.d.	n.d.	27.4	n.d.	n.d.	32.6	n.d.	n.d.	0.2	n.d.	0.2
Cr	0.7	n.d.	n.d.	n.d.	n.d.	n.d.	n.d.	n.d.	n.d.	n.d.	n.d.	n.d.	n.d.	n.d.	n.d.

Legend: n.d. - not detected

Table 3. Chemical composition of measured points by EDS

Compared to fired CM, fired CMV30 presents a denser structure with lower porosity (**Fig. 5c**). This is consistent with the thermal expansion/contraction result, which indicates a higher degree of vitrification. However, some large spherical or oval-shaped pores are developed in fired CMV30 (**Fig. 5c)**. In addition, vermiculite/vrm-bt retains a partial sheet-like morphology even at 1150 °C (**Fig. 5c**); some pores can be seen in this structure due to the exfoliation/expansion of vermiculite and vrm-bt. It is inferred that vermiculite may melt at 1000-1150 °C as Sutcu [13] reported the clear layer-structured expanded vermiculite flakes at 1000 °C. The identified minerals in fired CMV30, based on composition and with reference to bulk XRD analysis, are diopside (point 9), rutile (point 10), hematite (point 11), quartz/cristobalite (point 12), cordierite (point 14) and enstatite (point 15).

Fig. 5e and **5f** show SEM images of CMV30 buttons fired at 450 °C and 750 °C, which are onset and end temperatures of the exfoliation of vermiculite/vrm-bt (see area "4" in the dilatometric curve, **Fig. 4**). At 450 °C, vermiculite/vrm-bt exhibits a typical flake morphology with closely packed parallel layers. After 750 °C, a structure with pores between adjacent layers is observed. Large cracks are also developed beside the expanded flakes (**Fig. 5f**).

3.6. Physical, mechanical and thermal diffusivity properties

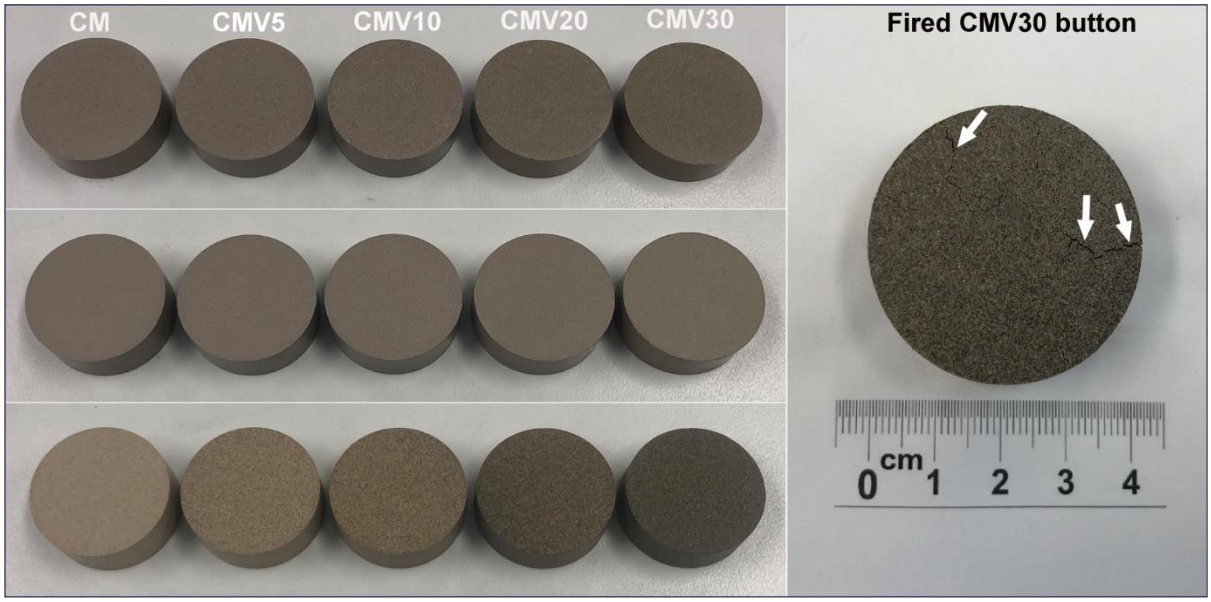

Fig. 6. The appearance of brick buttons at different stages of production. In the left image, top to bottom pictures: green bodies, dried brick buttons, and fired brick buttons

Appearance: For the green body and dried brick buttons, a consistent "coffee" colour is observed regardless of V addition (**Fig. 6**). This is because V and CM are both "buff" colour at around room temperature. However, the fired brick buttons become darker after V has been introduced. A change from "light camel" (fired CM) to "black olive" (fired CMV30) is presented, which is presumably related to the formation of the cordierite phase.

In addition, irregular cracks (~1 cm) appear on the surface of the fired CMV30 (white arrows, **Fig. 6** right), which may be caused by intense dimensional changes during firing (450-750 °C, 750-950 °C and 950-1150 °C, **Fig. 4**), since no cracks are observed in the green bodies and dried bricks. To determine the time of crack occurrence, different temperatures are selected to fire CMV30 with corresponding photographs shown in **Fig. 7**. This comparison indicates that cracks occur between 450-750 °C due to the exfoliation of vrm-bt and vermiculite. As the temperature rises, some cracks are compensated by vitrification and severe shrinkages at high temperatures, but they do not entirely disappear even after firing at 1150 °C.

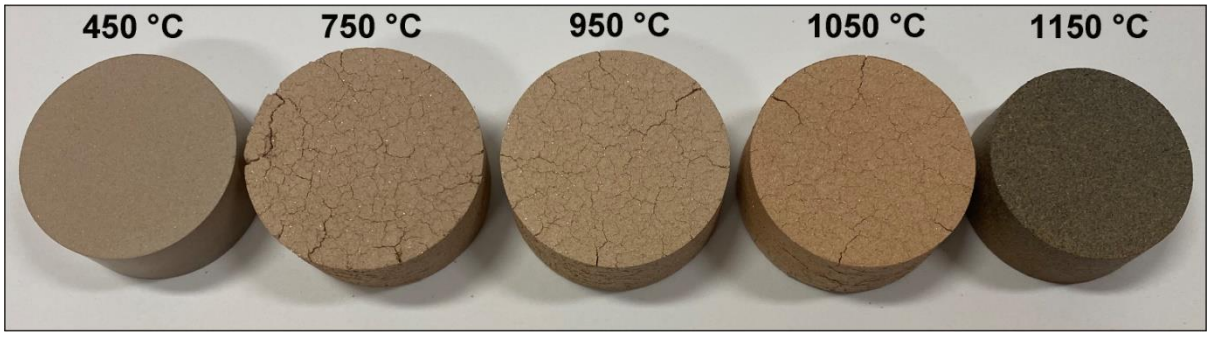

Fig. 7. The appearance of the CMV30 brick button fired at different temperatures

Porosity: Through a combination of water absorption experiments (a routine practice used by brick manufacturers) and N_2 isothermal adsorption and desorption measurement, the porosities of fired brick buttons were investigated (**Table 4**).

For the water absorption experiments, both CWA and BWA decrease from CM to CMV30, which indicates a lower porosity after the V-added samples have been fired. This result aligns with the higher shrinkage of these samples on the dilatometric curves (**Fig. 4a**). In addition, a downward trend of the saturation coefficient is observed with the increase of V content, which results in stronger freeze/thaw resistance for brick because a higher proportion of tiny pores (measured by BWA) can create more space for the expansive force of water freezing. However, it is worth emphasising that the water absorption experiment only covers pores of ~1-10 μm, so the large cracks in **Fig. 7** may not be included, as water tends to flow down in these cracks due to gravity [44]. In addition, for all samples, BET surface area and the average pore size show very close values at 2.16-2.61 g/cm^3 and 5.08-5.37 nm, respectively, indicating that the pores on the nanometre scale are consistent.

Fired samples	24 h cold water absorption (CWA, %)	5 h boiled water absorption (BWA, %)	Saturation coefficient (CWA/BWA)	BET surface area (m^2/g)	Average pore size* (nm)
CM	10.27	12.37	0.83	2.37	5.35
CMV5	9.13	11.63	0.78	2.48	5.30
CMV10	7.69	10.64	0.72	2.61	5.37
CMV20	6.92	10.50	0.66	2.31	5.22
CMV30	6.07	9.46	0.64	2.16	5.08

*Based on BET surface area analysis, limited to pores between 1.7 and 300 nm

Table 4. Cold and boiled water absorption and BET results for fired brick buttons

Shrinkage: In **Fig. 8a**, an apparent increase in both drying and firing shrinkage is observed with higher V content. The introduction of V by 5% has increased the drying shrinkage from 0.01% to 0.33%, which is caused by the removal of surface and interlayer water from vermiculite,

biotite and vrm-bt. In addition, the rate of drying shrinkage slows down when V is increased from 5% to 30%. In terms of the firing shrinkage, a significant increase occurs after 1010 °C with a rise in V addition (area "6", **Fig. 4a**). A greater extent of vitrification causes this because a higher concentration of clay minerals is in the starting materials. Furthermore, the clay mineral type affects the firing shrinkage. Clay minerals containing more fluxing elements (*e.g.*, K, Fe, Mg and Ca) more readily show a liquid-like morphology during firing than that with only Al and Si, such as kaolinite [42]. Since V in this study consists of vermiculite, vrm-bt and biotite, which are rich in Mg, Fe and K, while CM contains mainly kaolinite (34.6 wt.%), more viscous liquid forms in the V added clay mixtures, which results in stronger particle connections and shrinkage.

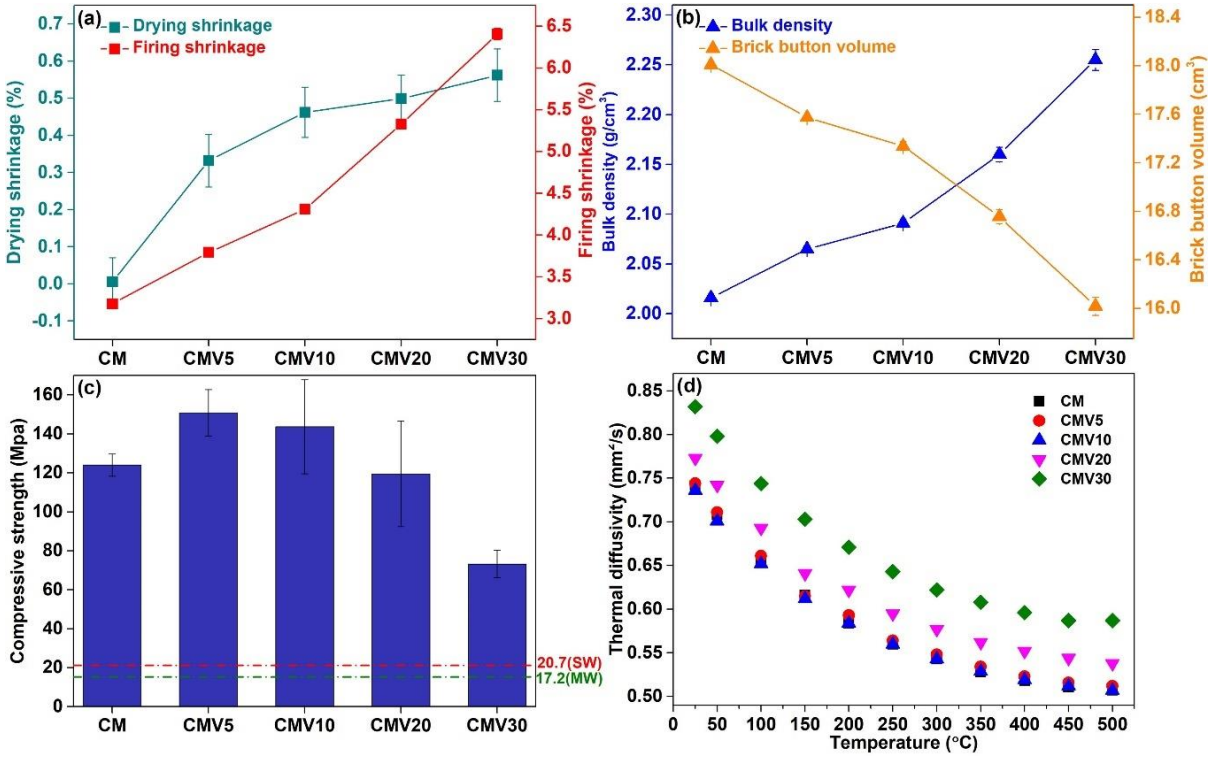

Fig. 8. Physical and mechanical properties of green bodies and brick buttons: drying and firing shrinkages (**a**), bulk density and brick button volume (**b**), compressive strength (**c**) and thermal diffusivity (**d**)

Density and volume: The weights of fired brick buttons are comparable according to weighing results using a digital scale. However, volumes have changed considerably (from 18.01 to 16.01 cm^3 for CM and CMV30, respectively, **Fig. 8b**) after incorporating V because of the continuous increase in drying and firing shrinkage. This has caused a linear increase in density from 2.02 (CM) to 2.07 (CMV5), 2.09 (CMV10), 2.16 (CMV20), 2.26 cm^3/g (CMV30), respectively. These values are higher than commonly reported in the literature (usually ≤ 2.00 cm^3/g) [13, 45] due to a higher sintering temperature used in this work.

Compressive strength: The compressive strength of the samples varied significantly depending on V addition. Strength values increase first then decrease with an increase of V content in the starting material (**Fig. 8c**). The highest and lowest values are 150.94 MPa and 73.33 MPa for CMV5 and CMV30, respectively. The addition of V affects mechanical properties in two aspects: 1) severe expansion at 450-750 °C as shown on the dilatometric curve in **Fig. 4**, which causes cracks and weakens the mechanical strength; 2) enhanced vitrification after 950 °C (**Fig. 4**), which promotes the strength [6]. This mechanism is also supported by an increase in firing shrinkage (**Fig. 8a**) and amorphous content in the products. The amorphous content increases from 27 wt.% (fired CM) to 30 wt.% (fired CMV5), 34 wt.% (fired CMV10), 45 wt.% (fired CMV20) and 47% wt.% (fired CMV30) with V addition, indicated by the quantitative XRD results in **Fig. S3**. Although CMV30 has the lowest water absorption value (**Table 4**), and SEM images show a denser structure of fired CMV30 than fired CM (**Fig. 5**), cracks on fired CMV30 can serve as starting points of failure, so the lowest compressive strength is still obtained. In comparison, the expansion between 450-750 °C in fired CMV5 is well offset by the metakaolin shrinkage (area "4" in the dilatometric curve, **Fig. 4a**), so a smooth transition is achieved with optimum mechanical performance due to higher vitrification. This result is different to that published in previous research which found a linear decrease of compressive strength, but with expanded vermiculite (*i.e.*, pre-fired before addition to starting materials) and a lower sintering

temperature (900-1000 °C) used [13, 14]. In this study, firing at 1150 °C more effectively utilises liquid-phase sintering caused by vitrification of vermiculite, vrm-bt and biotite, confirmed by the sharp shrinkage of V added clay mixtures at 950-1150 °C (**Fig. 4a)**, so a noticeable strength enhancement is obtained.

Thermal diffusivity: V additions at 20% and 30% in CM increase the thermal diffusivity of brick buttons by 5% and 15%, respectively. However, V additions at 5% and 10% do not significantly impact thermal diffusivity. This trend can be explained by the dilatometric curves in **Fig. 4a** - the total shrinkages of CMV5 and CMV10 only slightly increase compared to CM, while the shrinkages of CMV20 and CMV30 sharply rise. Since more shrinkage will result in a denser brick structure and reduced porosity [46], the thermal diffusivity could be improved significantly for fired CMV20 and CMV30 buttons.

In short, the higher firing temperature used in this study has resulted in higher compressive strength and lower water absorption than that of other products described in the literature [45, 47]. CM can be classified as a Grade MW brick (brick intended for use in moderate weathering areas), which requires a compressive strength larger than 17.2 MPa with water absorption and saturation coefficient less than 22% and 0.88, respectively [48]. CMV5, CMV10, CMV20 and CMV30 belong to a Grade SW brick (brick intended for use in a severe weathering area), which requires a compressive strength larger than 20.7 MPa with water absorption and saturation coefficient less than 17% and 0.78, respectively.

4. Conclusion

The addition of V at different dosages (0 wt.%, 5 wt.%, 10 wt.%, 20 wt.%, and 30 wt.%) significantly affects the thermal behaviours, physical and mechanical properties of fired brick buttons. Our experimental protocol and tools to determine these properties may provide helpful

guidance for brick production, primarily if vermiculite or vermiculite-biotite are present in the raw materials.

1) V in clay mixtures alters the nature and timing of phase transitions, including kaolinite dehydroxylation and rutile formation. Three Mg-containing phases are identified - antigorite (460 °C), enstatite (870 °C) and cordierite (1150 °C). Mullite, quartz and cristobalite are suppressed in V-added brick buttons, while the amorphous phase, enstatite and cordierite contents increase.
2) Between 25-1150 °C, five different weight loss steps and six dilatometric/contraction steps are defined. The addition of V not only brings a substantial expansion between 450-750 °C but shrinkage after 950 °C is also exacerbated due to the modified content and species of clay minerals.
3) The vermiculite and vermiculite-biotite retain a partial sheet-like morphology with pores at 1150 °C. V has changed the colours of brick buttons from “light camel” (fired CM) to “black olive” (fired CMV30) due to the formation of cordierite. Expansion/exfoliation of vermiculite and vermiculite-biotite causes cracks on fired CMV30 surface. In addition, the drying shrinkage, firing shrinkage and density rise considerably with V addition. The compressive strength increases first and then drops. A maximum value reaches 150.94 MPa (a rise of 21.6% compared with the control sample) when the V content is 5 wt.%. Also, the thermal diffusivity remains unchanged at this dosage. Therefore, 5 wt.% of raw, untreated V is considered an optimum ratio to add into a clay mixture for brick production.

Acknowledgments

This work is funded by an Advance Queensland Research Fellowship (Grant No. AQRF01716-17RD2). The authors would like to acknowledge Mr Mike Newitt, Mr Calum Henderson and Mr Mick Bolton from Brickworks Ltd., Mr Donald McAuley and Miss Karine Harumi Moromizato from the Central Analytical Research Facility (CARF) for their assistance with sample characterisations.

References

[1] F. Bergaya, G. Lagaly, **General Introduction: Clays, Clay Minerals, and Clay Science**, Handbook of Clay Science, 1 (2006), pp. 1-18, 10.1016/S1572-4352(05)01001-9

[2] L.Y. Zhang, **Production of bricks from waste materials - A review**, Constr. Build. Mater., 47 (2013), pp. 643-655, 10.1016/j.conbuildmat.2013.05.043

[3] S. Guzlena, G. Sakale, S. Certoks, L. Grase, **Sand size particle amount influence on the full brick quality and technical properties**, Constr. Build. Mater., 220 (2019), pp. 102-109, 10.1016/j.conbuildmat.2019.05.170

[4] M.V. Vasic, L. Pezo, J.D. Zdravkovic, Z. Backalic, Z. Radojevic, **The study of thermal behavior of montmorillonite and hydromica brick clays in predicting tunnel kiln firing curve**, Constr. Build. Mater., 150 (2017), pp. 872-879, 10.1016/j.conbuildmat.2017.06.068

[5] S. Freyburg, A. Schwarz, **Influence of the clay type on the pore structure of structural ceramics**, J. Eur. Ceram. Soc., 27 (2-3) (2007), pp. 1727-1733, 10.1016/j.jeurceramsoc.2006.04.158

[6] S. Wang, L. Gainey, D. Baxter, X.D. Wang, D.R.I. Mackinnon, Y.F. Xi, **Thermal behaviours of clay mixtures during brick firing: A combined study of in-situ XRD, TGA and thermal dilatometry**, Constr. Build. Mater., 299 (2021), p. 124319, 10.1016/j.conbuildmat.2021.124319

[7] M.V. Vasic, L.L. Pezo, Z. Radojevic, **Optimization of adobe clay bricks based on the raw material properties (mathematical analysis)**, Constr. Build. Mater., 244 (2020), 10.1016/j.conbuildmat.2020.118342

[8] V.T. Shmuradko, F.I. Panteleenko, O.P. Reut, E.F. Panteleenko, N.V. Kirshina, **Composition, structure, and property formation of heat insulation fire- and heat-reflecting materials based on vermiculite for industrial power generation**, Refract. Ind. Ceram., 53 (4) (2012), pp. 254-258, 10.1007/s11148-012-9503-5

[9] G.W. Brindley, G. Brown, **Crystal Structures of Clay Minerals and their X-Ray Identification**, Mineralogical Society of Great Britain and Ireland(1980)

[10] S. Hillier, E.M.M. Marwa, C.M. Rice, **On the mechanism of exfoliation of 'Vermiculite'**, Clay Miner., 48 (4) (2013), pp. 563-582, 10.1180/claymin.2013.048.4.01

[11] B. Beal, A. Selby, C. Atwater, C. James, C. Viens, C. Almquist, **A Comparison of Thermal and Mechanical Properties of Clay Bricks Prepared with Three Different Pore-Forming Additives: Vermiculite, Wood Ash, and Sawdust**, Environ. Prog. Sustain., 38 (6) (2019), p. 13150, 10.1002/ep.13150

[12] A.M. Rashad, **Vermiculite as a construction material - A short guide for Civil Engineer**, Constr. Build. Mater., 125 (2016), pp. 53-62, 10.1016/j.conbuildmat.2016.08.019

[13] M. Sutcu, **Influence of expanded vermiculite on physical properties and thermal conductivity of clay bricks**, Ceram. Int., 41 (2) (2015), pp. 2819-2827, 10.1016/j.ceramint.2014.10.102

[14] Angel Georgiev, Albena Yoleva, Stoyan Djambazov, Dimitar Dimitrov, V. Ivanova, **Effect of expanded vermiculite and expanded perlite as pore forming additives on the physical properties and thermal conductivity of porous clay bricks**, J. Chem. Technol. Metall., 53 (2) (2018), pp. 275-280

[15] ASTMC67/C67M, **Standard Test Methods for Sampling and Testing Brick and Structural Clay Tile,** ASTM International, West Conshohocken, PA, USA (2020), 10.1520/C0067_C0067M-20

[16] Y. Maniatis, M.s. Tite, **Technological examination of Neolithic-Bronze age pottery from central and southeast Europe and from the Near East**, J. Archaeol. Sci., 8 (1981), pp. 59-76, 10.1016/0305-4403(81)90012-1

[17] D.L. Whitney, B.W. Evans, **Abbreviations for names of rock-forming minerals**, Am. Mineral., 95 (1) (2010), pp. 185-187, 10.2138/am.2010.3371

[18] C.E. White, J.L. Provis, T. Proffen, D.P. Riley, J.S.J. van Deventer, **Combining density functional theory (DFT) and pair distribution function (PDF) analysis to solve the structure of metastable materials: the case of metakaolin**, Phys. Chem. Chem. Phys., 12 (13) (2010), pp. 3239-3245, 10.1039/b922993k

[19] V.A. Drits, G. Besson, F. Muller, **An improved model for structural transformations of heat-treated aluminous dioctahedral 2:1 layer silicates**, Clays Clay Miner., 43 (6) (1995), pp. 718-731, 10.1346/Ccmn.1995.0430608

[20] P.R.L. Welche, V. Heine, M.T. Dove, **Negative thermal expansion in beta-quartz**, Phys. Chem. Miner., 26 (1) (1998), pp. 63-77, 10.1007/s002690050161

[21] G. Cultrone, C. Rodriguez-Navarro, E. Sebastian, O. Cazalla, M.J. De La Torre, **Carbonate and silicate phase reactions during ceramic firing**, Eur. J. Mineral., 13 (3) (2001), pp. 621-634, 10.1127/0935-1221/2001/0013-0621

[22] P.K. Gallagher, D. Johnson Jr, **The effects of sample size and heating rate on the kinetics of the thermal decomposition of CaCO3**, Thermochim. Acta, 6 (1) (1973), pp. 67-83, 10.1016/0040-6031(73)80007-3

[23] Y. Wang, W.J. Thomson, **The Effect of Sample Preparation on the Thermal-Decomposition of Caco3**, Thermochim. Acta, 255 (1995), pp. 383-390, 10.1016/0040-6031(94)02151-D

[24] G. Spinola, U. Anselmi-Tamburini, **Mechanism of low temperature calcite decomposition**, Solid State Ionics, 26 (2) (1988), p. 175

[25] G. Cultrone, F.J.C. Rosua, **Growth of metastable phases during brick firing: Mineralogical and microtextural changes induced by the composition of the raw material and the presence of additives**, Appl. Clay Sci., 185 (2020), p. 105419, 105419 10.1016/j.clay.2019.105419

[26] G. Cultrone, I. Aurrekoetxea, C. Casado, A. Arizzi, **Sawdust recycling in the production of lightweight bricks: How the amount of additive and the firing temperature influence the physical properties of the bricks**, Constr. Build. Mater., 235 (2020), p. 117436, 10.1016/j.conbuildmat.2019.117436

[27] H. Schneider, K. Okada, J.A. Pask, **Mullite and mullite ceramics**, John Wiley & Sons Chichester, England, New York, Brisbane, Toronto, Singapore (1994)

[28] Y.F. Wang, Y.G. Tang, S.Q. Liu, Y.G. Wang, R.B. Finkelman, B.L. Wang, X. Guo, **Behavior of trace elements and mineral transformations in the super-high organic sulfur Ganhe coal during gasification**, Fuel Process. Technol., 177 (2018), pp. 140-151, 10.1016/j.fuproc.2018.04.019

[29] C. Rodriguez-Navarro, G. Cultrone, A. Sanchez-Navas, E. Sebastian, **TEM study of mullite growth after muscovite breakdown**, Am. Mineral., 88 (5-6) (2003), pp. 713-724, 10.2138/am-2003-5-601

[30] L.Y. Ma, X.L. Su, Y.F. Xi, J.M. Wei, X.L. Liang, J.X. Zhu, H.P. He, **The structural change of vermiculite during dehydration processes: A real-time in-situ XRD method**, Appl. Clay Sci., 183 (2019), p. 105332, 105332 10.1016/j.clay.2019.105332

[31] S.M. Johnson, J.A. Pask, J.S. Moya, **Influence of Impurities on High-Temperature Reactions of Kaolinite**, J. Am. Ceram. Soc., 65 (1) (1982), pp. 31-35, 10.1111/j.1151-2916.1982.tb09918.x

[32] M. Valaskova, Z. Klika, B. Novosad, B. Smetana, **Crystallization and Quantification of Crystalline and Non-Crystalline Phases in Kaolin-Based Cordierites**, Materials, 12 (19) (2019), p. 3104, 310410.3390/ma12193104

[33] B.A.E.-K. Ahmed M. Yahyaa, Abdel Monem M. Soltana, Sayed H. Kenawyb, Esmat M. A. Hamzawyc, **Cordierite ceramic through glass and ceramic routes from kaolin and talc**, Egypt. J. Chem., 64 (4) (2021), pp. 1751-1758, 10.21608/EJCHEM.2021.53853.3115

[34] D.A.H. Hanaor, C.C. Sorrell, **Review of the anatase to rutile phase transformation**, J. Mater. Sci., 46 (4) (2011), pp. 855-874, 10.1007/s10853-010-5113-0

[35] X.C. Zuo, D. Wang, S.L. Zhang, Q.F. Liu, H.M. Yang, **Intercalation and Exfoliation of Kaolinite with Sodium Dodecyl Sulfate**, Minerals, 8 (3) (2018), p. 112, 10.3390/min8030112

[36] S. Wang, X.C. Zuo, H.F. Cheng, Y.J. Yang, Q.F. Liu, **Structural Model and De-Intercalation Kinetics of Kaolinite-Methanol-Sodium Stearate Intercalation Compound**, J. Braz. Chem. Soc., 27 (7) (2016), pp. 1311-1318, 10.5935/0103-5053.20160136

[37] E. Post, J.B. Henderson, Characterization of Two Different Clay Materials by Thermogravimetry (TG), Differential Scanning Calorimetry (DSC), Dilatometry (DIL) and Mass Spectrometry (MS)-12215, Germany WM Conference, Germany, 2012.

[38] F. Bergaya, P. Dion, J.F. Alcover, C. Clinard, D. Tchoubar, **TEM study of kaolinite thermal decomposition by controlled-rate thermal analysis**, J. Mater. Sci., 31 (19) (1996), pp. 5069-5075, 10.1007/Bf00355907

[39] Y. Takashi, T. Tomoyuki, H. Tetsuo, **Dependence of luminescence sensitivities of quartz on alpha-beta phase inversion break temperatures**, Radiat. Meas., 41 (7-8) (2006), pp. 841-846, 10.1016/j.radmeas.2006.05.008

[40] H.F. Muiambo, W.W. Focke, M. Atanasova, A. Benhamida, **Characterization of urea-modified Palabora vermiculite**, Appl. Clay Sci., 105 (2015), pp. 14-20, 10.1016/j.clay.2014.12.019

[41] A. Gualtieri, M. Bellotto, **Modelling the structure of the metastable phases in the reaction sequence kaolinite-mullite by X-ray scattering experiments**, Phys. Chem. Miner., 25 (6) (1998), pp. 442-452, 10.1007/s002690050134

[42] C.J. McConville, W.E. Lee, **Microstructural development on firing illite and smectite clays compared with that in kaolinite**, J. Am. Ceram. Soc., 88 (8) (2005), pp. 2267-2276, 10.1111/j.1551-2916.2005.00390.x

[43] A.F. Gualtieri, **Thermal behavior of the raw materials forming porcelain stoneware mixtures by combined optical and In situ X-ray dilatometry**, J. Am. Ceram. Soc., 90 (4) (2007), pp. 1222-1231, 10.1111/j.1551-2916.2007.01614.x

[44] P. Nieminen, M. Romu, **Porosity and Frost-Resistance of Clay Bricks**, Bri. Blo. Mason., 1-3 (1988), pp. 103-109,

[45] P. Munoz, V. Letelier, M.A. Bustamante, J. Marcos-Ortega, J.G. Sepulveda, **Assessment of mechanical, thermal, mineral and physical properties of fired clay brick made by mixing kaolinitic red clay and paper pulp residues**, Appl. Clay Sci., 198 (2020), p. 105847, 10.1016/j.clay.2020.105847

[46] R.F. Li, Y. Zhou, C.W. Li, S.B. Li, Z.Y. Huang, **Recycling of industrial waste iron tailings in porous bricks with low thermal conductivity**, Constr. Build. Mater., 213 (2019), pp. 43-50, 10.1016/j.conbuildmat.2019.04.040

[47] Munib Ul Rehman, Madiha Ahmad, K. Rashid, **Influence of fluxing oxides from waste on the production and physico-mechanical properties of fired clay brick: A review**, J. Build. Eng., 27 (2020), p. 100965, 10.1016/j.jobe.2019.100965

[48] ASTMC62, **Standard Specification for Building Brick (Solid Masonry Units Made From Clay or Shale),** ASTM International, West Conshohocken, PA, USA (2017), 10.1520/C0062-17